

## NICMOS CORONAGRAPHIC OBSERVATIONS OF 55 CANCRI

G. SCHNEIDER

Steward Observatory, University of Arizona, Tucson, AZ 85721; gschneider@as.arizona.edu

E. E. BECKLIN

Department of Physics and Astronomy, University of California at Los Angeles, Los Angeles, CA 90095

B. A. SMITH

Institute for Astronomy, University of Hawaii, Honolulu, HI 96822

A. J. WEINBERGER

Department of Physics and Astronomy, University of California at Los Angeles, Los Angeles, CA 90095

AND

M. SILVERSTONE AND D. C. HINES

Steward Observatory, University of Arizona, Tucson, AZ 85721

Received 2000 September 21; accepted 2000 October 10

### ABSTRACT

We present new near-infrared ( $1.1\ \mu\text{m}$ ) observations of the circumstellar environment of the planet-bearing star 55 Cancri. With these *Hubble Space Telescope* (*HST*) images we are unable to confirm the observation of bright scattered radiation at longer NIR wavelengths previously reported by Trilling and coworkers. NICMOS coronagraphic images with detection sensitivities to  $\sim 100\ \mu\text{Jy arcsec}^{-2}$  at  $1.1\ \mu\text{m}$  in the region 28–60 AU from the star fail to reveal any significant excess flux in point-spread function (PSF) subtracted images taken in two *HST* orbits. These new observations place flux densities in the 19–28 AU zone at a factor of 10 or more below the reported ground-based observations. Applying a suite of a dozen well-matched coronagraphic reference PSFs, including one obtained in the same orbits as the observations of 55 Cnc, yielded consistently null results in detecting a disk. We also searched for and failed to find a suggested flux-excess anisotropy in the ratio of  $\sim 1.7:1$  in the circumstellar background along and orthogonal to the plane of the putative disk. We suggest that, if such a disk does exist, then the total  $1.1\ \mu\text{m}$  spectral flux density in an annular zone 28–42 AU from the star must be no more than  $\sim 0.4\ \text{mJy}$ , at least 10 times smaller than suggested by Trilling and Brown, upon which their very large estimate for the total dust mass ( $0.4\ M_{\oplus}$ ) was based. Based on the far-infrared and submillimeter flux of this system and observations of scattered light and thermal emission from other debris disks, we also expect the intensity of the scattered light to be at least an order of magnitude below our upper limits.

*Key words:* circumstellar matter — stars: individual (55 Cancri)

### 1. INTRODUCTION

The connection between the formation and growth of planetesimals into larger bodies and the circumstellar debris disks around young and nascent stars from which they arise has been the subject of continual speculation, discussion, and inquiry, since the original scenario for such evolution was first expanded upon by Laplace (1796), following the general proposition by Kant (1755). With the imaging of the  $\beta$  Pictoris circumstellar disk by Smith & Terrile (1984), as originally detected by *IRAS* (Aumann 1985), this paradigm of the formation of planetary systems became more visceral. The observation and direct imaging of such circumstellar disks, seen in scattered light surrounding other stars and exhibiting morphologically resolved spatial features in the near-infrared (NIR), have recently been reported; e.g., HR 4796A (Schneider et al. 1999), HD 141569 (Weinberger et al. 1999), TW Hydrae (Weinberger et al. 2000). The expectation for imaging dust disks around such stars was hopeful, given their relatively large thermal infrared excesses. The detection and imaging of possible circumstellar material around stars having little or no thermal infrared or submillimeter radiation was presumed to be much more difficult. Nonetheless, a survey of solar-like, planet-bearing stars as ascertained from radial

velocity surveys was conducted by Trilling & Brown (1998, henceforth TB98) who reported on the detection of a bright dust disk seen in scattered light around 55 Cancri.

55 Cancri ( $\rho^1$  Cnc, HR 3522, HD 75732, G8 V,  $d = 12.53$  pc,  $V = 5.93$ ; Marlborough 1964),  $H = 4.17$  (Persson, Aaronson, & Frogel 1977), R.A. =  $08^{\text{h}}52^{\text{m}}36^{\text{s}}.13$ , decl. =  $+28^{\circ}19'53''.0$  (J2000.0, epoch 1991.25) is an older star ( $\sim 5$  Gyr, Baliunas et al. 1997) for which a planetary companion of  $M \sin i = 0.84\ M_{\text{Jup}}$  was found by Butler et al. (1997) in their radial velocity search for exosolar planets (Marcy & Butler 1994). With a somewhat peculiar spectrum, Cowley, Hiltner, & Witt (1967) classified it as G8 V and hence “solar-like.” More recently Baliunas et al. (1997) found its spectrum more closely resembled a subgiant and reclassified it as G8 II–III, although a search through the literature spanning more than four decades (e.g., Nikonov et al. 1957, Marlborough 1964, and others) reveals no evidence of any optical variability as may be expected at some level for a subgiant. Gonzalez (1998) confirmed its subgiant luminosity reclassification but noted that its theoretical-isochrone age is anomalous. Further, they tentatively suggest the presence of an unresolved binary companion orbiting nearly pole-on and that their results are consistent with a gas giant planet encroaching very close to the star and accreting H- and

He-depleted material onto the photosphere. A period of 14<sup>d</sup>65 was ascribed to the planetary companion by Butler et al. (1997). At a distance of 12.53 pc, as determined by Hipparcos, the companion orbits with a semimajor axis of 0.12 AU and eccentricity of 0.03.

TB98 reported the detection of a disk using near-infrared coronagraphic imaging at 1.62, 2.12, and 2.28  $\mu\text{m}$ , using the cold coronagraph (CoCo)/NSFCAM (Toomey et al. 1998) with a 1.5 radius mask at the IRTF. The maximum *H*-band brightness of the disk was given as  $\sim 1 \text{ mJy arcsec}^{-2}$  at a radius of 2". The disk reported was asymmetric in the sense that the total flux density in quadrants described to be along the major axis was  $\sim 70\%$  higher than the flux in the minor axis quadrants. The radial decrease in brightness was found to follow a  $r^{-5}$  power law and the inferred mass in dust was  $0.4 M_{\oplus}$ . Trilling, Brown, & Rivkin (2000, henceforth TBR2000) later suggested that a flux density peak in *H*-band might approach  $3 \text{ mJy arcsec}^{-2}$ , as discussed in the context of a survey of six stars with known radial velocity companions.

Evidence for the detection of a Vega-like disk at 60  $\mu\text{m}$  with a flux excess of  $170 \pm 30 \text{ mJy}$  was reported by Dominik et al. (1998) from ISOPHOT observations with no detection at either 25  $\mu\text{m}$  or longer (95, 160, 185  $\mu\text{m}$ ) wavelengths, from which they inferred a disk radius of  $\sim 50 \text{ AU}$ . The corresponding  $L_{\text{disk}}/L_{*}$  at 60  $\mu\text{m}$  is  $6 \times 10^{-5}$ , implying 2 orders of magnitude less dust than in other disks seen in scattered NIR light, as discussed above. Recently, Jayawardhana et al. (2000, henceforth JAY2000) reported a submillimeter excess of  $7.5 \pm 4.2 \text{ mJy}$  at 450  $\mu\text{m}$  and, more significantly,  $2.8 \pm 0.5 \text{ mJy}$  at 850  $\mu\text{m}$ , as determined from SCUBA/JCMT observations. They attributed this excess to thermal emission from a dust population resembling our Kuiper Belt. The amount of dust required to produce these submillimeter fluxes is, again, 2 orders of magnitude below the dust seen in the previously noted near-infrared scattered light disks. Mid-IR (10.8 and 18.2  $\mu\text{m}$ ) images obtained by JAY2000 using the University of Florida's OSCIR camera on Keck II showed no excess emission above the stellar photospheric level.

In an attempt to confirm and further characterize the reported NIR scattered light disk we have imaged the circumstellar environment of 55 Cnc at four wavelengths with the coronagraph in the Near-Infrared Camera and Multi-object Spectrometer (NICMOS) on the *Hubble Space Telescope* (*HST*). Given the sensitivities routinely achieved by NICMOS differential coronagraphy, we had anticipated

detecting and imaging the disk readily at the  $\sim 2''$  limiting radius of the CoCo observations based on the flux levels reported by TB98. From our NICMOS observations, however, we are unable to confirm the existence of a NIR flux excess in our most sensitive (1.1  $\mu\text{m}$ ) images at flux density levels an order of magnitude lower than those reported by TB98.

## 2. OBSERVATION

Near infrared coronagraphic observations of 55 Cnc were obtained on 1998 November 1 with four filters (Table 1) in NICMOS camera 2 (image scale:  $X = 0''.0760 \text{ pixel}^{-1}$ ,  $Y = 0''.0753 \text{ pixel}^{-1}$ ) in two *HST* orbits (see Table 2). The star was occulted in the 0.3 radius coronagraphic hole, 3.4 and 5.5 from the ( $-X$ ,  $+Y$ ) corner of the  $19''.46 \times 19''.28$  field of view. After acquiring the target into the low-scatter point of the coronagraphic system, repeated MULTIACCUM imaging sequences were executed at two field orientations (spacecraft roll angles constrained by available guide stars) differing by  $15^{\circ}$ .

The imaging strategy for this two-orbit observation differed somewhat from that which we routinely employed for other targets in our *HST*/NICMOS disk and companion search programs (Lowrance et al. 1998). Those single-orbit, single-color, observations were designed as the initial detection phase of an unbiased multiple target survey. Here, in this two-orbit observation, we were attempting to confirm and further characterize the disk reported by TB98. At the first field orientation a deep-imaging sequence was executed at 1.1  $\mu\text{m}$ , where the residual instrumental scatter in the coronagraph is minimized by the small size of the PSF relative to that of the coronagraphic hole (Schneider et al. 1998b). At the same orientation, images were also obtained

TABLE 1  
SPECTRAL FILTERS AND PHOTOMETRIC CALIBRATIONS

Filter	$\lambda_{\text{cent}}$ ( $\mu\text{m}$ )	FWHM ( $\mu\text{m}$ )	mJy $\text{ADU}^{-1} \text{ s}^{-1}$	Zero Point <sup>a</sup>
F110W .....	1.0985	0.5920	2.031	1775
F160W .....	1.5960	0.4030	2.190	1083
F187N <sup>b</sup> .....	1.8740	0.0192	41.07	825
F204M .....	2.0313	0.1050	7.711	735
F237M .....	2.3978	0.1975	4.913	635

<sup>a</sup> Janskys for 0 Vega magnitude.

<sup>b</sup> Used for target acquisition.

TABLE 2  
NICMOS CORONAGRAPHIC EXPOSURE LOG

Target	Filter	UT Start	Sequence	Reads	$N^a$	Exp. (s)	Integ. (s) <sup>b</sup>	Orient. (deg) <sup>c</sup>
55 Cnc .....	F110W	05:21:31	STEP32	11	13	95.96	1247.5	42.5
55 Cnc .....	F204M	05:35:49	STEP32	10	4	63.96	255.8	42.5
55 Cnc .....	F240W	05:40:56	STEP64	11	5	127.96	639.8	42.5
55 Cnc .....	F110W	06:48:20	STEP32	11	4	95.96	383.8	57.5
55 Cnc .....	F160W	06:55:31	STEP64	12	1	191.96	192.0	57.5
HD 75216 .....	F110W	07:14:14	STEP32	11	4	95.96	383.8	57.5
HD 75216 .....	F110W	07:22:13	STEP32	10	5	63.96	319.8	57.5

<sup>a</sup> Number of repeated MULTIACCUM exposures.

<sup>b</sup> Total Integration time for that filter/orientation.

<sup>c</sup> Angle of image + *Y*-axis eastward of celestial north.

at 2.04 and 2.40  $\mu\text{m}$  to provide additional color information on the disk. In the following orbit the spacecraft was rolled by  $15^\circ$  and additional 1.1  $\mu\text{m}$  images were obtained to discriminate between artifacts induced by the *HST* + NICMOS optical system and true circumstellar features. In the second orbit we also acquired a short 1.6  $\mu\text{m}$  image to allow us to directly compare the morphological and photometric properties of the putative disk in the same spectral region as reported by TB98. In the same orbit the spacecraft was then slewed a small distance ( $\sim 1.3^\circ$ ) to obtain images to construct a contemporaneous 1.1  $\mu\text{m}$  PSF from a reference star, HD 75216 (SAO 80447, PPM 99074, K2III),  $V = 7.38$ ,  $H = 4.60$ , R.A. =  $08^{\text{h}}49^{\text{m}}45^{\text{s}}.32$ , decl. =  $+29^\circ26'56''.2$  (J2000.0, epoch 1991.25), with a spectral type and brightness similar to 55 Cnc.

### 3. DATA REDUCTION

The individual reads in each raw MULTIACCUM image (Mackenty 1997) were dark subtracted, corrected for non-linearities in pixel responses, flat-fielded, and combined into a count-rate image (counts  $\text{s}^{-1}$  pixel $^{-1}$ ) employing an analog to the CALNICA software used in the STScI data pipeline. Calibration reference files (STEP32 and STEP64 dark frames and flat fields for the filters employed) prepared by the NICMOS instrument definition team (IDT) were used in processing the images, rather than library reference files supplied by STScI. The reference flat fields were augmented with renormalized data from contemporaneous lamp calibration images (obtained as part of the target acquisition process) to permit calibration very close to the edge of the coronagraphic hole, since its position in the NICMOS focal plane is known to vary slightly with time. Bad pixels were replaced in the count-rate images by two-dimensional Gaussian-weighted interpolation of neighbor pixels with radii appropriate for the wavelengths of the different filters. Each reduced set of images with the same target, filter and orientation was then median combined into a single image. Known artifacts induced by the readout electronics, such as broad “stripes” orthogonal to the readout direction and localized elevated count levels at the locations of deeply exposed targets, both replicated in all four detector quadrants, were characterized and removed. Count rates were converted to physical flux densities based on photometric calibrations derived as part of the overall instrumental calibration by the NICMOS IDT (M. J. Rieke 1999, private communication), as shown in Table 1.

### 4. PSF-SUBTRACTED IMAGES (1.1 $\mu\text{m}$ )

We have searched our 55 Cnc images obtained in all four spectral bands (Table 1) for evidence of light scattered by circumstellar material. In this paper we discuss only our 1.1  $\mu\text{m}$  observations, which afford the greatest sensitivity for disk detection, as the stray light rejection of the NICMOS coronagraph performs best at short wavelengths. The NICMOS coronagraph itself reduces the intensity of the background light by factors of a few to about 10 within a few arcseconds of an occulted star. The unapodized edge of the  $0.3$  radius coronagraphic hole, however, acts both as a diffracting aperture and as a scattering surface caused by microroughness in manufacture, and it is the primary source of instrumental contamination. The FWHM of the PSF (which scales linearly with wavelength) is  $\sim 0''.12$  at 1.1  $\mu\text{m}$ , and hence the F110W PSF is well contained within the

hole. When a star is centered in the coronagraph, F110W light from just beyond the second Airy minimum of the PSF falls on the hole edge and is reduced in intensity by a factor of  $\sim 250$  with respect to the peak. This is  $\sim 6$  times greater reduction in relative intensity at the hole edge with respect to the peak than is obtained in *H*-band with the F160W filter. Thus, to maximize the disk-to-star contrast ratio by reducing the background scattered and diffracted light, the F110W filter is the spectral element of choice. Our longer wavelength observations were planned assuming a disk surface brightness suggested by TB98. It appears, however, that the scattered-light disk must be substantially fainter than had been reported (see § 7.1). Hence, our longer wavelength images were of insufficient sensitivity to meaningfully contribute to an investigation of the disk reported by TB98 and TBR2000, and we do not discuss them further.

Because of the brightness of 55 Cnc itself relative to a surrounding dust disk, a reference PSF must be subtracted in order to reveal any low-contrast circumstellar flux. The efficacy of subtracting NICMOS coronagraphic PSFs from coronagraphic targets has been discussed at length (e.g., Schneider 1998a). The NICMOS PSF can exhibit small changes in the mid- and high-frequency structures on multi-orbit timescales, which result from thermal instabilities in the heating of the *HST* secondary mirror support (Bely 1993) and from very small movements of the cold mask with respect to the detector (Krist et al. 1998).<sup>1</sup> The effects of these variations may be minimized by obtaining a reference PSF within an interval shorter than the thermal time constant of the *HST* optical telescope assembly (OTA). To this end we imaged HD 75216, a nearby bright star of similar color, to serve as a primary reference PSF. These data were obtained at nearly the same spacecraft attitude and in the same visibility period as the second of two contiguous orbits of 1.1  $\mu\text{m}$  observations.

The HD 75216 images were reduced and calibrated in the same manner as the 55 Cnc images. The photometrically calibrated PSF image was subtracted from the 55 Cnc images at each of the two field orientations after spatial registration and flux-scaling. Coronagraphic image registration was accomplished by means of cubic convolution interpolation (Park & Schowengerdt 1983) using the IDP3 program (Lytle et al. 1999) developed by the NICMOS IDT. The target locations “behind” the coronagraph were ascertained by measuring the unocculted target centroids (via Gaussian profile matching) in the calibrated acquisition

<sup>1</sup> The *HST* + NICMOS PSF is complex, in part because of a misalignment of the Lyot stop at the cold pupil, leading to striated structures in the energy redistributed radially along the OTA spider vanes and secondarily diffracted by the edges of the spider mask. Because of small (subpixel) instabilities in the position of the cold mask with respect to the *HST* pupil (known as “wiggles”; see Krist et al. 1998) on both suborbit timescales and with secular drifts over weeks or months, the energy along the spikes is not always completely nulled by subtracting a reference PSF taken either at a different phase of the orbit or at a different epoch. The residual energy along the spikes is radially distributed, essentially, as the difference of two  $J_2$  Bessel functions. These often exhibit modulations in intensity over spatial scales of tens of pixels arising from very small secular variations in the OTA focal length, due to uncompensated desorption of the optical bench and from suborbital changes due to “breathing” (see Bely 1993). Thus, it is not always possible to null the integrated energy along the  $45^\circ$  and  $225^\circ$  diffraction spikes simultaneously, nor to zero the total energy, particularly when a PSF taken at epoch different from the target is applied. As this would bias any azimuthal averaging, we mask these regions in making all circumferential measurements discussed in this paper.

images and then applying the down-linked acquisition slew offsets executed by the NICMOS flight software in the coronagraphic acquisition process. Flux-scaling of the PSF was accomplished by iteratively nulling the diffracted energy in the difference images along the OTA spider vanes while demanding that the adjacent background at large radii remain zero. The sensitivity of the residual background to the PSF flux scaling is discussed by Weinberger et al. (1999), and we elaborate further in § 6.

The resulting pair of PSF-subtracted images of 55 Cnc is shown in Figure 1. The image in panel (a) was obtained at a spacecraft orientation angle of  $42^{\circ}5$  (first orbit, visit 60), such that the major axis of the disk reported by TB98 would lie essentially along the vertical. In panel (b) the field was rotated  $15^{\circ}$  “clockwise” around the occulted star. Image artifacts in the optical system arising from scattered and diffracted starlight rotate with the detector and are essentially invariant. While such artifacts remain spatially fixed, any circumstellar light rotates with the field, and hence an asymmetric disk would appear to rotate  $15^{\circ}$  about the target between image *a* and image *b*. The region interior to a distance of  $\sim 25$  AU (26.5 pixels, or  $\sim 2''$ ), represented by the green circles in Figure 1, is largely dominated by residual scattered light from the star. This is just interior to the inner boundary of the radial region fit by TB98, beyond which they report confidence that their data were unaffected by the presence of the  $1''.5$  radius occulting mask in the CoCo instrument. The dashed yellow circle corresponds to a radius of 42 AU, the outermost region for which TB98 confidently reported measuring a  $1.6 \mu\text{m}$  flux excess. Hence, the annulus between the green and yellow circles is the region considered in detail by TB98, in which they show an asymmetric disk with an  $r^{-5}$  power-law drop off in the surface brightness profile.

##### 5. SELECTION OF REFERENCE PSFs

The measurement uncertainties in the circumstellar flux densities are dominated by image artifacts in the imperfect

subtractions of reference PSFs. These uncertainties set the detection limits for a disk and are a strong function of radial distance from the occulted star. Near the star the NICMOS measurements are dominated by the residual systematic error in nulling out the imperfectly matched PSFs. While the  $1 \sigma$  pixel-to-pixel noise in spatial regions far from the influence of circumferential diffracted and instrumentally scattered light is typically  $\sim 0.2 \mu\text{Jy arcsec}^{-2}$ , this is not germane in assessing the detectability of a disk where the sensitivities are ultimately limited by the much larger systematics in the presence of the PSF-subtraction residuals.

We have assessed our detection limits for our 55 Cnc images in two ways, as we have for other targets in the NICMOS IDT Environments of Nearby Stars (EONS) program (Schneider 1998a). First we looked at the noise statistics of the circumstellar backgrounds following the registration, flux scaling, and subtraction of a suite of well-matched reference PSFs. We also examined the dispersion in the flux densities in equal-radii annular zones measured from each of the PSF-subtracted images. Second we implanted a model disk with the characteristics described by TB98 into PSF subtracted target and flux-scaled reference images to see how well a disk of this nature would have been detected. To validate our results, in addition to applying the contemporaneous HD 75216 reference PSF that was obtained specifically for this purpose, we used 11 other PSFs obtained in the same manner in our observing program (see Table 3). We restricted our reference PSFs to stars observed within 10 weeks of the 55 Cnc observation to obviate any concerns of small secular instabilities in the NICMOS instrument over longer timescales. Most of these stars were themselves candidates for possessing scattered light disks (with the exceptions of HD 75216 and HR 4748). None of these, however, have shown any evidence of scattered light flux excesses in the spatial region of interest and hence were retained as reference PSFs. In particular  $\epsilon$  Eridani and  $\tau^1$  Eridani were excellent choices, as they were both significantly brighter than 55 Cnc (yielding very high

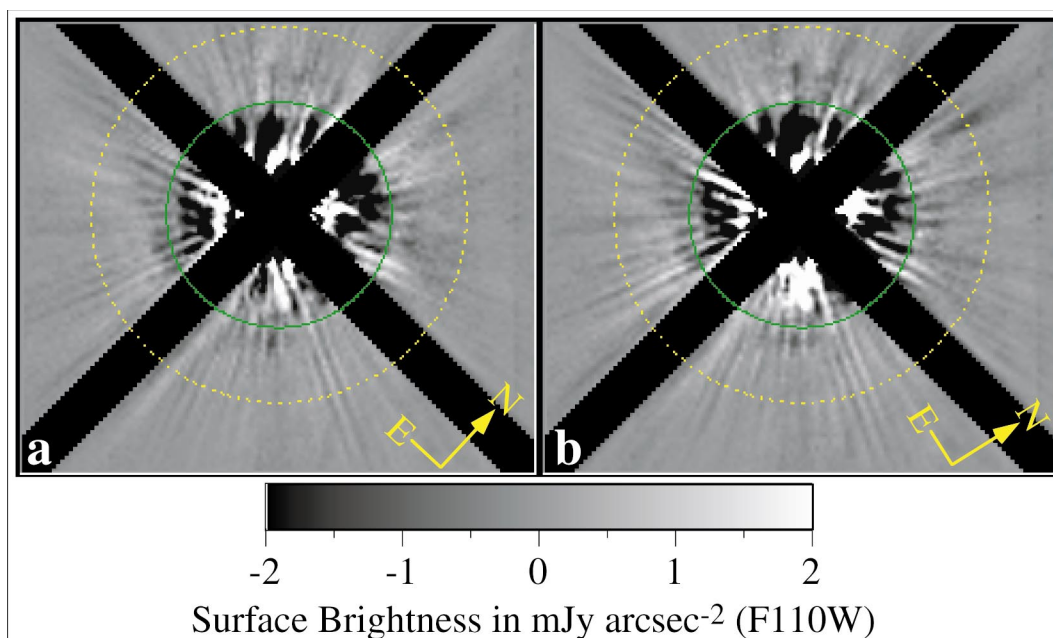


FIG. 1.—PSF-subtracted F110W coronagraphic images of the circumstellar region in the vicinity of 55 Cnc in two successive *HST* orbits with a flux-renormalized PSF of HD 75216 subtracted. The fields shown are  $9''$  wide. (a) North, in the left image, is to the upper right ( $42^{\circ}5$  from vertical, nearly along the diffraction-spike mask). (b) With the reorientation of the telescope, the field as has been rotated  $15^{\circ}$  clockwise with respect to the image in panel (a).

TABLE 3  
REFERENCE PSFs FROM NICMOS GTO/7226 (N418)

Star	Visit	Sp.	$H$ (mag)	Obs. Date
<i>HD 75216</i> .....	62	<i>K2 III</i>	4.60	1998 Nov 1
$\tau^1$ <i>Eri</i> .....	80	<i>F5 V</i>	3.35	1998 Nov 14
$\tau^1$ <i>Eri</i> .....	81	<i>F5 V</i>	3.35	1998 Nov 14
$\epsilon$ <i>Eri</i> .....	03	<i>K2 V</i>	1.6	1998 Sep 26
$\tau^1$ <i>Eri</i> .....	18	<i>F5 V</i>	3.35	1998 Sep 24
$\epsilon$ <i>Eri</i> .....	04	<i>K2 V</i>	1.6	1998 Sep 26
UX ORI .....	11/12	<i>A2 Ve</i>	7.95	1998 Nov 4
49 CET .....	14/15	<i>A1 V</i>	5.59	1998 Nov 7
VEGA .....	73	<i>A0 V</i>	0.03	1998 Nov 9
HR 4748 .....	92	<i>B8 V</i>	5.44	1998 Aug 16

signal-to-noise PSFs) and observed at more than one spacecraft orientation angle. We hasten to note that, while  $\epsilon$  Eri has a known excess in the thermal IR and a dust ring detected in the submillimeter, this is at very large angular radii ( $\sim 20''$ – $30''$ ), as reported by Greaves et al. (1998), and thus far outside the region of interest.

We were unable to detect any statistically significant circumstellar flux in either of the 55 Cnc images with any of the twelve reference PSFs used. We consider separately the circumferential flux reported in the 28–42 AU annular zone by TB98 which they fitted to an  $r^{-5}$  power law, and the more complex surface brightness profile and peak flux density reported in the 19–28 AU zone by TBR2000. For both zones the contemporaneous HD 75216 PSF worked best in minimizing the subtraction residuals and introduced the least amount of structural artifacts in both orientations of 55 Cnc images (visits 60 and 61) at radii greater than  $\sim 25$  AU, yielding nearly identical null results (see § 6). Similar null results, although with somewhat less statistical significance, were obtained using the other reference PSF stars listed in Table 3, where stars with two visit numbers on the same date were observed at two spacecraft roll angles. We discuss in detail the results obtained using four observations of the first three stars (of spectral types F–K to minimize small color effects within the bandpass of the F110W filter)

listed in italics in Table 3. We compare these with a very similar null result obtained using HR 4748. This star was chosen because it has no evidence of, nor any expectations for, either a surrounding disk or detectable companions.

## 6. SUBTRACTION SENSITIVITIES TO STELLAR FLUX ESTIMATES

Potentially, circumstellar brightness profiles measured from PSF-subtracted images may be affected by either under- or over-subtracting the reference PSF. Aperture photometry of PSF cores of coronagraphically occulted target and reference stars is not possible. Thus, we measure the flux densities in many corresponding regions along the unocculted diffraction spikes of the target and reference star PSFs at radii beyond where a disk may be present to establish the stellar flux density ratios. For well-exposed, contemporaneous images the photometric flux density ratios derived from this approach are very robust. Typically, we find that the dispersion in the measurements from different positions along the four diffraction spikes lead to uncertainties in the flux ratios of  $< 1\%$ . The 55 Cnc (visit 61) and HD 75216 (visit 62) images, shown in Figure 2, were obtained closely together in the same *HST* orbit and at the same spacecraft roll orientation. The  $1\sigma$  uncertainty in the determined flux ratio of 2.51:1 is 0.6% (6 millimag). This process does not work as well when using PSFs taken at different epochs, because of small changes in the PSF structures from secular instabilities in the *HST* focus and the NICMOS/*HST* optical interface. In such cases and for the other PSFs employed as given in Table 3, errors of up to a few percent are typical. As a check, we required that the flux ratios agreed with expectations based upon aperture photometry from unocculted target acquisition images transformed to the F110W band within their measurement and transformation uncertainties.

The common problem arising from misestimates in stellar flux ratios is the introduction of artifacts in PSF-subtracted images. Such artifacts induce departures in the morphology and amplitude of the circumstellar light arising from the combination of diffraction and instrumental scattering due to a point source (i.e., a star without a disk). If the

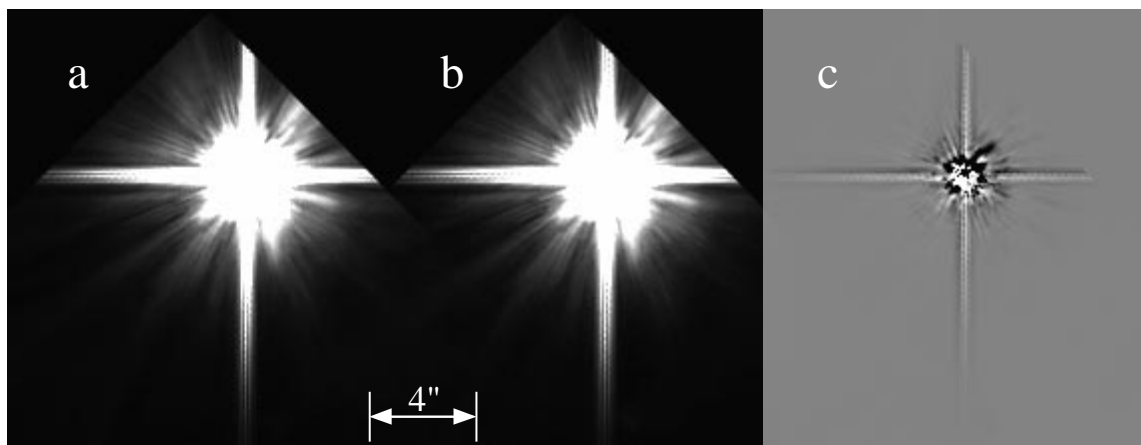


FIG. 2.—NICMOS F110W coronagraphic images of 55 Cnc (a) and HD 75216 (b) flux scaled by a factor of 2.51 by ratioing the intensities of the light from the diffraction spikes of (a) and (b) as described in the text. Systematic instabilities give rise to slightly different structures in the two PSFs, resulting in the residuals seen in the difference image (c). Panels (a) and (b) are stretched over a dynamic range of 0 to 0.1 mJy pixel $^{-1}$ . Panel (c) is a bipolar stretch from  $-0.1$  to 0.1 mJy pixel $^{-1}$  (same positive domain) to illustrate the nature of the subtraction residuals. The images have been rotated  $45.5^\circ$  clockwise to place the diffraction spikes along the horizontal and vertical, so north is to the right (and slightly up) in panel (a).

brightness of the subtracted reference PSF is overestimated, an artifact resembling a circumstellar disk may arise. We quantify the magnitude of this effect for properly PSF-subtracted NICMOS F110W coronagraphic images of unresolved point sources in the  $2''.3 < r < 3''.3$  annular zone where 50% of the total area, along the orthogonal diffraction spikes, has been excluded with an oversized mask. Typically, a 1% change in the brightness of a flux-matched reference PSF of flux density,  $F$ , will result in a change in the integrated flux density of the instrumentally scattered light of  $\sim 1.5 \times 10^{-5} F$  into this region.

Here we consider the inverse possibility, that the reference PSFs employed and/or their flux-density scaling were biased in such a way as to suppress the visibility of intrinsic circumstellar scattered radiation. Therefore, to assess the efficacy of the PSF subtractions for 55 Cnc, we performed identical image reductions and subtractions for control stars (i.e., stars without known or expected disks) whose F110W flux densities were renormalized to that of 55 Cnc

( $\sim 46$  Jy) to serve as comparative nulls. Reference PSFs were flux-scaled to the renormalized null stars by simultaneously demanding that the variance of the residual flux in the diffraction-spike-masked images was minimized while the total flux density approached zero within the uncertainties imposed by estimating the flux ratios from the diffraction-spike fluxes.

We then estimated the sensitivity of the circumstellar-flux-nulling process to misestimates in the stellar flux by adjusting the scaling factor of the reference PSFs by known amounts and then seeing how that affected the circumferential flux densities. As an example, in Figure 3 we show three PSF subtractions of HR 4748, a control star with no detectable disk or companions, using HD 75216 as a reference PSF. Figure 3a is the best result, having used the flux-matching criteria discussed. The morphology of this image may be compared with the PSF-subtracted images of 55 Cnc in Figure 1. A small (and inconsequential) “softening” of the HR 4748 image is noticeable because of a minor focus

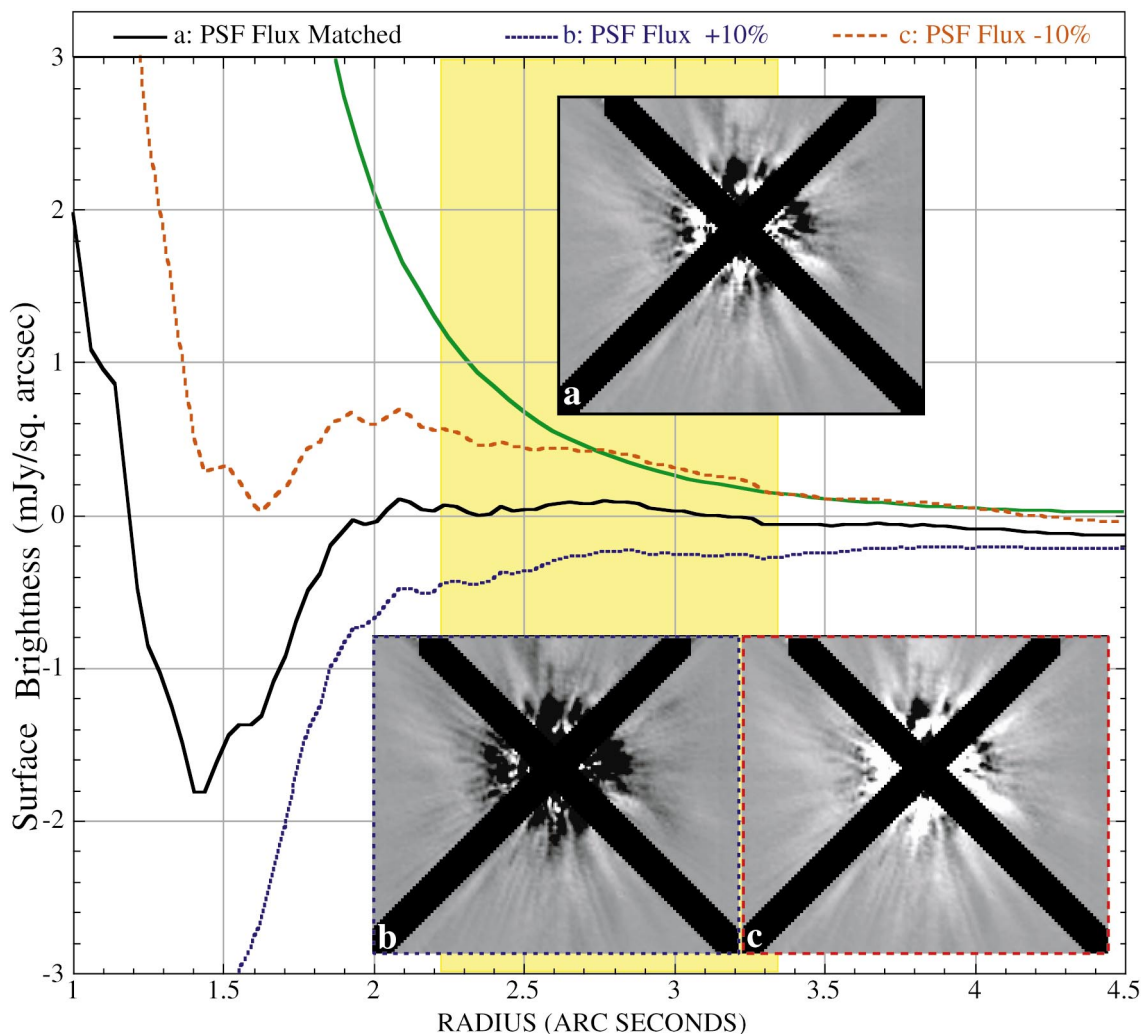


FIG. 3.—Incorrect estimates of target and reference star brightness affect the morphological structure and measured circumstellar flux in PSF-subtracted images. Inset (a) represents a “best” image of the null source HR 4748, where the reference PSF (HD 75216, obtained contemporaneously with the 55 Cnc images) was subtracted by variance-minimized nulling of the circumferential flux (based upon measured stellar flux ratios checked with band-transformed photometry from target acquisition images). Under- and over-subtracted images, by 10% in the F110W reference star flux, are shown for PSF-subtracted images of HR 4748 (insets [b] and [c]). These PSF-subtracted images of the null source may be compared with those of 55 Cnc in Fig. 1. Azimuthally averaged radial profiles measured from these images are also shown and may be compared with the top panels in Fig. 4. Radial zones at the same angular distances considered for 55 Cnc by TB98 (and discussed in § 7.1) are indicated by the yellow background. The green line indicates an  $r^{-5}$  surface brightness profile suggested by TB98 and fitted to the 55 Cnc data presented in Fig. 3 of TBR2000 (renormalized to F110W as discussed in the text).

shift in the *HST*/OTA between the two observational epochs, and this effectively smooths the image over a scale of  $\sim 2$  pixels. Nonetheless, the instrumentally scattered and diffracted light in the properly flux-scaled image is highly spatially correlated with the 55 Cnc images, suggesting the absence of any circumferential flux due to a disk.

As an example of flux mis-scaling, Figures 3b and 3c show the effects of increasing and decreasing the flux density of the HD 75216 reference PSF by 10% (an arbitrary illustrative amount) before subtraction. The resulting under- and over-subtractions in the PSF-subtracted images of HR 4748 are readily apparent, not only in the inner regions in these images ( $< 2''$  from the star), but also further out in the regions of particular interest ( $2''.3 < r < 3''.3$ ) in the corresponding radial profiles. The total flux density measured in this diffraction-spiked-masked annular zone (corresponding to the 28 to 42 AU region around 55 Cnc discussed by TB98) is  $0.52 \pm 0.36$  mJy (standard deviation of all pixels) for the “best” subtraction for HR 4748. This imperfect nulling implies that there is a small bias due to unresolved systematics in this subtraction. In the case of the 10% undersubtraction, we find a flux excess artifact of  $5.61 \pm 0.40$  mJy and a deficit of  $-4.59 \pm 0.38$  mJy for the 10% oversubtraction. These flux density artifacts imply a scattered light rejection ratio of  $\sim 1 \times 10^{-4}:1$  into the masked annulus for the 10% misestimates of the reference star flux densities. This approximately agrees with the expectation for  $1.5 \times 10^{-5}$  rejection into this annulus from a 1% mis-scaling for typical coronagraphic performance.

In the case of the PSF-subtracted image of 55 Cnc (visit 61) using HD 75216 (the same reference PSF as for the above null source), we measured an integrated flux density in the masked 28 to 42 AU region of  $+0.40$  mJy after correcting for the masked area (§ 7.1). Changing the flux density of HD 75216 in the subtraction by  $\pm 0.6\%$ , the  $1 \sigma$  uncertainty in the flux ratios, gives rise to uncorrected flux density measurements of  $+0.21$  and  $+0.18$  mJy. But the TB98 results would have predicted a flux density in the masked annulus of  $4.0$  mJy, a factor of  $\sim 20$  higher than that seen in our visit 61 image. Suppression of  $3.8$  mJy of flux in the masked annulus from a  $46$  Jy source due to a flux mis-scaling of the reference PSF would have required a photometric error of  $\sim 8\%$  in establishing the 55 Cnc: HD 75216 F110W brightness ratios, a factor of 13 higher than our estimated uncertainty. For the 55 Cnc (visit 60) image, taken in an earlier orbit at a different spacecraft roll orientation, the flux ratio to the same reference PSF was found to be  $2.52 \pm 0.023$  ( $0.9\% 1 \sigma$ ). The increase in the uncertainty in the flux-scaling by 50% was due to secular changes in the 55 Cnc PSF between the two orbits. These data resulted in a higher integrated flux density of  $+0.32$  mJy measured in the masked annulus, which remains an order of magnitude lower than that suggested by TB98. These measures are consistent with the typical scattered light rejection properties of the NICMOS coronagraph at  $1.1 \mu\text{m}$  and strongly suggest that we did not inadvertently null a bright disk by oversubtracting reference PSFs.

Finally, we examine the radial profiles resulting from under-, over-, and properly scaled subtractions of the reference PSF (HD 75216) from the null source (HR 4748) and compare them with the  $r^{-5}$  profile suggested for 55 Cnc by TB98 (*green line*, Fig. 3). We note that it is possible to null the integrated flux density of a TB98-like disk by severely oversubtracting a reference PSF. However, the radial mor-

phology of the disklike artifact produced by an under-subtraction of the same magnitude has a complex radial morphology, which bears *no resemblance* to an  $r^{-5}$  dependency in the same angular radial zone considered by TB98.

## 7. FLUX DENSITIES

High spatial frequency radial artifacts (“streaks”) in the PSF-subtracted images, at azimuthal scales comparable to single pixels, contaminate the images at small radii. As the error in the background measurement at a given radial distance is due to azimuthal variations in intensity; these well-known image artifacts cause an overestimation in the formal measurement error. To mitigate the radial artifacts to some degree, we measure the brightness profiles (discussed in §§ 7.1 and 7.2) after applying a  $3 \times 3$  pixel smoothing kernel to the difference images. This spatially degrades the resolution by a factor of 2 to  $\sim 0''.23$ , but it smooths over the high spatial frequency artifacts, thus yielding a better estimate of the uncertainty in the larger scale backgrounds at smaller radii.

### 7.1. The 28–42 AU Zone

For each of the PSF subtractions we measured the total flux density enclosed in an annulus between 28 and 42 AU, the annular zone fit by TB98. In doing so we excluded pixels along the diffraction spikes and in two small regions where scattered light artifacts are known to be induced by the coronagraphic optics. The resultant region, where observations were made, included 1495 pixels covering  $8.6 \text{ arcsec}^2$ . We correct the measured total flux densities in the masked annulus by a factor of 2.06, linearly scaling the measured flux by the ratio of areas in unmasked to masked annuli. The integrated flux densities, corrected for the unsampled areas, are presented in Table 4 along with their error estimates (standard deviation over all pixels) for each of the subtractions.

Our ability to measure the integrated flux density in this region has an internal accuracy of  $\sim 0.08$  mJy when subtracting any of the noncontemporaneous PSFs, or  $\sim 0.05$  mJy when using the HD 75216 PSF obtained contiguously with the 55 Cnc observations. However, as is evident, the flux densities measured among these representative PSF subtractions have a dispersion of about  $\pm 0.9$  mJy. This is indicative of the fact that, as an ensemble, the measures are dominated by systematics in the subtractions themselves. These systematics arise primarily from uncertainties in the flux-scaling of the reference PSFs, but they also result from structural variations among the PSFs used. The HD 75216 (visit 62) PSF was taken in the same target visibility period (shorter than the thermal time constant of the

TABLE 4  
INTEGRATED FLUX DENSITIES (mJY)

PSF	55 Cnc Visit 60	55 Cnc Visit 61
V62.....	$+0.66 \pm 0.046$	$+0.40 \pm 0.058$
V81.....	$+0.23 \pm 0.075$	$+0.02 \pm 0.074$
V80.....	$-1.26 \pm 0.093$	$-1.48 \pm 0.084$
V03.....	$+0.88 \pm 0.080$	$+0.72 \pm 0.077$
Model TB98 Disk: <sup>a</sup> 8.2 mJy (F110W; $28 < r < 42$ AU)		

<sup>a</sup> Flux( $r$ ) =  $1.24 (r/28 \text{ AU})^{-5}$  mJy arcsec $^{-2}$  on major axis, sinusoidally modulated azimuthally with 1.7:1 axial flux ratio.

NICMOS + *HST* focal plane variations) as the visit 61 images of 55 Cnc. The resulting difference image is the most free of optical artifacts at distances  $\gtrsim 2''$  induced by PSF mismatches (see § 6). The uncertainty in the flux scaling of this PSF to the 55 Cnc images (both visits) was smaller by a factor of 2 than for any other PSF. Thus, a priori, we expected this to be the “best”-matched PSF (most devoid of systematics), and this was found to be the case based upon the criteria already discussed. Given the systematic uncertainties, we cannot say if the +0.4 mJy integrated density of the circumstellar flux seen in the visit 61–visit 62 image is wholly instrumentally scattered flux or if there is an underlying disk component which may be below our detection threshold. Allowing for the 0.6% uncertainty in the flux-scaling and the internal measurement error of 0.06 mJy (see Table 4), we would be unable to detect a disk-integrated flux density of  $\lesssim 0.4 \pm 0.07$  mJy. The F110W flux density of 55 Cnc itself is  $\sim 46$  Jy, implying a instrumental scattered light rejection ratio of  $\sim 10^5$  within this radial zone for these observations.

In Figure 4 we show the azimuthally averaged surface brightness profiles for the two 55 Cnc images using HD 75216,  $\epsilon$  Eri, and  $\tau^1$  Eri (at two spacecraft roll angles observed contiguously in one visibility period) as reference PSFs. These profiles exclude the imperfectly nulled diffraction spikes, which are masked in the accompanying images. The surface brightness profiles, measured in 1 AU wide radial increments, were determined after modestly smoothing the PSF-subtracted images as discussed in § 7. The  $1\sigma$  error bars indicate the standard deviation of all unmasked pixels in each incremental radius about the mean value at that radius,  $\sigma(N)$  and not the standard deviation of the mean,  $\sigma(\text{mean})$ . If the data in each pixel in an annulus were uncorrelated (i.e., independent) then  $\sigma(\text{mean})$  would simply be  $\sigma(N)/\sqrt{N}$ . Image artifacts at spatial frequencies of several pixels result in partial correlations of measured intensities in adjacent pixels in the difference images, particularly at smaller radial distances to the star. Thus,  $\sigma(\text{mean})$  approaches  $\sigma(N)/\sqrt{N}$  at large radii, but it becomes more uncertain at smaller radii in a complex manner.

We have characterized the major-axis flux densities for the disk suggested by TB98 (*green lines*, Fig. 4) as  $F(r) = 1.24 (r/28 \text{ AU})^{-5}$  mJy arcsec $^{-2}$ , where we have renormalized the TB98 *H*-band spectral flux densities to compare with our NICMOS F110W measures. Here we assume neutral gray scattering by the circumstellar grains at these wavelengths and hence the dust would take on the color of 55 Cnc. We believe this is a reasonable assumption for dust debris particles, which are likely to have a characteristic size of at least a few microns. We have found relatively neutral scattering in other debris disks observed by NICMOS in the F110W and F160W (very close to *H*) photometric bands (e.g., HR 4796A, Schneider et al. 1999; HD 141569, Weinberger et al. 1999, and Augereau et al. 1999; and TW Hya, Weinberger et al. 2000). We estimate the NICMOS F110W/*H* spectral energy density ratio of 55 Cnc using the STSDAS CALCPHOT routine to be  $\sim 1.20$  plus or minus a few percent, given the inherent uncertainties in the color transformation. In doing so we employ a Kurucz model atmosphere with an effective photospheric temperature of 5336 K,  $\log g = 4.3$ , and a metallicity of [0.45] dex above solar, all in accordance with both Gonzalez & Vanture (1998) and Fuhrmann, Pfeiffer, & Bernkopf (1998).

Integrating the reported  $r^{-5}$  profile (TB98), the expected total flux density in this region from a TB98-like disk is 8.2 mJy. This is a factor of 20 times higher than the  $\sim 0.4$  mJy detection limit that we derived using our best reference PSF (HD 75216), or more conservatively an order of magnitude higher than a limit based on the variations from the ensemble of PSF-subtracted images. We rule out the possibility of not detecting this much flux due to oversubtraction of our PSF stars, as detailed in § 6.

## 7.2. The 19–28 AU Zone

TBR2000 report measurable flux densities to within  $\sim 19$  AU of 55 Cnc, at the inner usable radius of CoCo system, which were not presented by TB98 in their initial analysis of the same data. TBR2000 more recently inferred a peak *H*-band surface brightness of the circumstellar light of  $\sim 3$  mJy arcsec $^{-2}$  near the edge of the  $1''.5$  radius coronagraphic mask at  $\sim 20$  AU (Fig. 3 of TBR2000). Although the TB98 power-law fit indicates that the surface brightness is apparently continuing to rise as  $r^5$  toward smaller radii there is an obvious roll-off in the surface brightness profile at  $r < 28$  AU, as presented by TBR2000. We reproduce their measured radial surface brightness profile (renormalized to the NICMOS F110W band as discussed in § 7.1) along with an extrapolation of the suggested  $r^{-5}$  profile for radii between 19 and 30 AU in Figure 5. An abrupt discontinuity in the TBR2000 surface brightness at  $r \approx 21$  AU is also seen where the circumferential flux density is an order of magnitude lower than the  $\sim 3$  mJy arcsec $^{-2}$  reported at 20 AU (or  $\sim 4$  mJy arcsec $^{-2}$  in NICMOS F110W). It is difficult to attribute this large amplitude variation as being intrinsic to the source, as it occurs over a much smaller spatial scale than the size of the best IRTF/CoCo seeing disk of  $0''.4$  (5 AU at the distance of 55 Cnc) reported by TBR2000. We suggest that this discontinuity and the reported  $\sim 3$  mJy arcsec $^{-2}$  *H*-band peak might arise from scattered light artifacts within the CoCo/IRTF optical system. Neither of these are seen in the NICMOS data where the size of a resolution element in the camera 2 F110W coronagraphic PSF is  $0''.12$  ( $\sim 1.6$  AU) sampled with  $0''.076$ -square pixels. TRB2000 copresent a similarly observed radial brightness profile for  $\nu$  Andromedae as a comparative null. We note, however, a very similar rise toward smaller radii in the  $\nu$  And circumferential brightness profile at nearly the same angular radial distance and magnitude as indicated for 55 Cnc. Unfortunately, TBR2000 do not present the data in the null profile at radii  $< 28$  AU, which makes comparing the morphology of the brightness profile of their control star to that of 55 Cnc difficult in the regions of highest reported circumstellar flux.

In the 25–30 AU region, where the TBR2000 measurements begin to diverge from the TB98  $r^{-5}$  power-law fit, we obtain a null result in detecting a disk to the levels of our sensitivity imposed by the systematics with flux densities of  $0.17 \pm 0.22$  mJy arcsec $^{-2}$  at 25 AU and  $0.04 \pm 0.12$  mJy arcsec $^{-2}$  at 30 AU. At the same distances TBR2000 suggest brightnesses of  $\sim 2$  and 1 mJy arcsec $^{-2}$ , respectively. These flux densities exceed the NICMOS determined upper limits by factors of 12 and 25 in the same radial zones, respectively, as we also saw for the integrated flux densities in the 28 AU  $< r < 40$  AU region. This suggests that, if a disk with flux densities reported by TB98 and TRB2000 was present in the 19–28 AU annular zone, it should also have been readily visible in the NICMOS images.



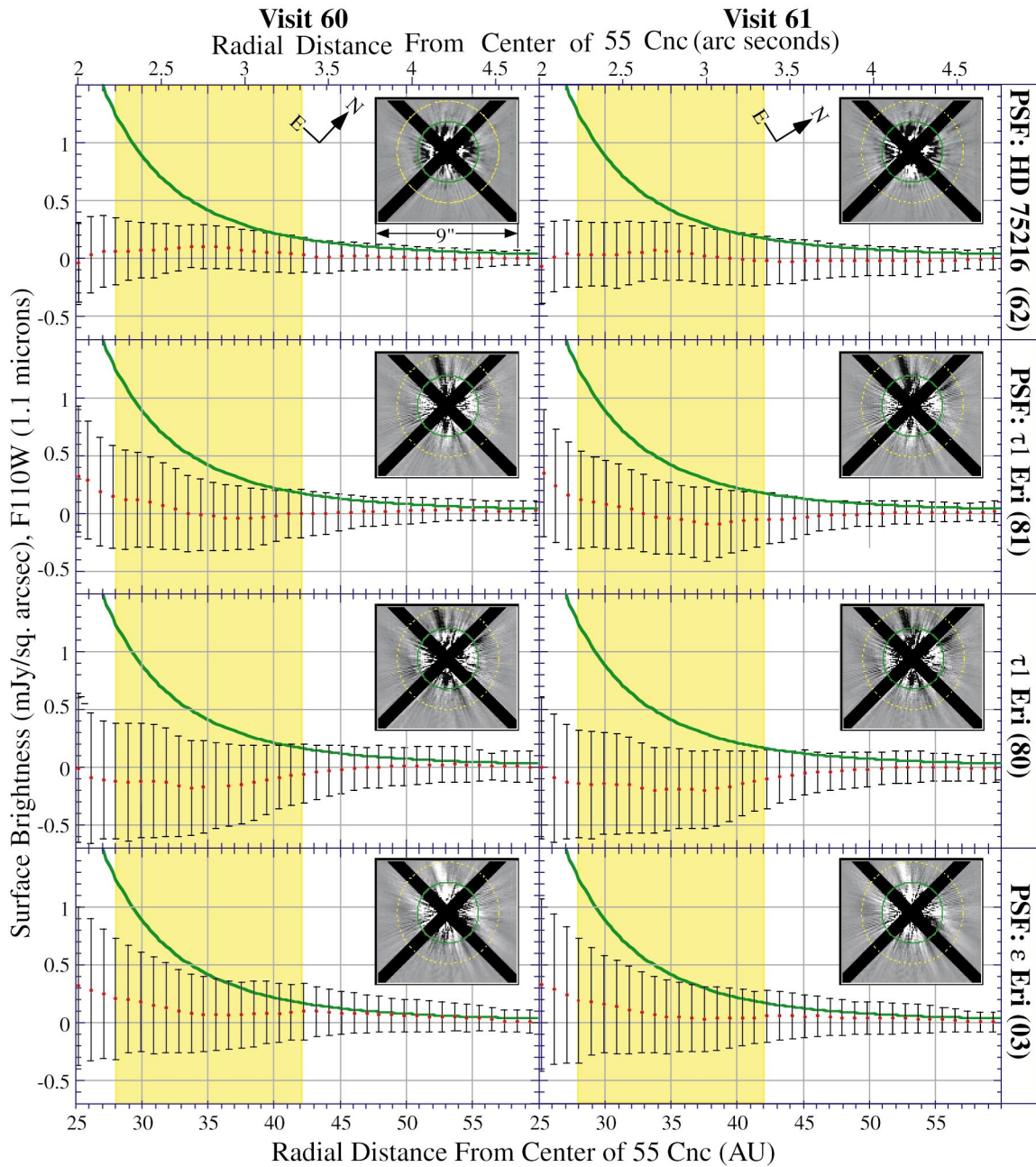


FIG. 4.—Azimuthally averaged F110W ( $1.1 \mu\text{m}$ ) surface brightness profiles<sup>2</sup> measured from PSF-subtracted images of 55 Cnc at two field orientations using four of our 12 reference PSFs. The images shown in the insets were smoothed as described in § 7.1 before computing the brightness profiles. The error bars indicate the standard deviations about the mean of all good pixels in each 1 AU wide annular zone. The putative 55 Cnc disk is oriented vertically between the masked diffraction spikes in the visit 60 image (*left*) and is rotated  $15^\circ$  clockwise in the visit 61 image (*right*). The yellow regions correspond to the radial zones considered by TB98. As in Fig. 3, the TB98/TBR2000 suggested  $r^{-5}$  power-law fit, adjusted for the NICMOS F110W bandpass, is indicated by the green line in each panel. The inset images from which the profiles were derived are stretched, scaled, and annotated as in Fig. 1 ( $\pm 2 \text{ mJy arcsec}^{-2}$  and  $9''$  wide, 25 and 42 AU zonal regions indicated).

<sup>2</sup> In measuring these profiles we also masked small regions which are known to be repeatedly affected by image artifacts in these radial zones at approximately “11 o’clock” and “2 o’clock” in the frame of the detector. The artifacts are obvious in the inset images (where they are unmasked only for illustrative purposes). In the  $\tau^1$  Eri PSF subtractions they appear as negative, whereas in the  $\epsilon$  Eri PSF subtractions they are positive, while they are not so obvious in the HD 75216 subtraction. The cause for the parity reversal is understood to be due to the “breathing” of the *HST* focal plane. The  $\tau^1$  Eri and  $\epsilon$  Eri PSFs were both slightly afocal with respect to the 55 Cnc image, but shifted in opposite directions, causing a phase inversion upon subtraction in these scattered light artifacts. Other implications for the effects of OTA focus changes due to breathing on NICMOS images are discussed in detail by Kulkarni et al. (2000).

## 8. MODEL DISK IMPLANTATION

Since we failed to find any circumstellar light above the level of the instrumental artifacts in the (imperfect) PSF subtractions, we then investigated how readily a disk with the photometric properties and morphology suggested by TB98 could have been detected in our images. To assess this we built a simple model disk characterized as described in § 7.1 and consistent with the TB98 results. To replicate the suggested major-to-minor-axis flux density ratio of 1.7:1 we sinusoidally varied the intensity of the disk azimuthally.

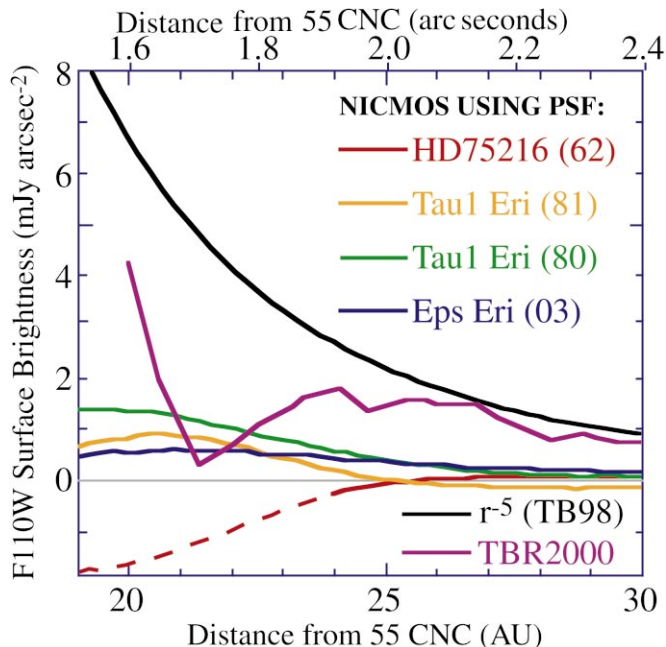


FIG. 5.—19–30 AU diffraction-spike-masked azimuthally averaged surface brightness measurements from several NICMOS PSF subtracted images of 55 Cnc presented along with the TBR2000 profile (renormalized to F110W, see text § 7.1) and an extrapolation of the TB98  $r^{-5}$  power-law fit to their data at radii interior to 28 AU. For illustrative purposes we show the results for the visit 60 image of 55 Cnc using the same reference PSFs as in Fig. 4, though similar results are obtained using our other previously discussed PSFs (Table 1) and for the visit 61 data. When applied to the visit 60 data the visit 62 PSF is a poor match at radii less than  $\sim 2''$  (dotted region,  $< 23$  AU) due to the thermal history of the telescope assembly and the relative phasing of these observations with the *HST* orbit as discussed by Schultz, Storrs, & Fraquelli (1999) and give rise to the anomalous (and nonphysical) negative residuals in this PSF subtraction at these radii which are rejected.

We then implanted a registered noiseless image of the model disk, with the major axis at a P.A. =  $42^\circ 5'$  (vertical in our visit 60 image and corresponding closely to the TBR2000 indicated orientation), into our PSF subtracted images of 55 Cnc. After implantation, we fully recovered the 8.2 mJy of superposed flux from the model disk measured in the same manner as the PSF-subtracted images of observed stars. This is a factor of about 20 higher than the measures using our contemporaneous PSF subtractions. The model disk implantation suggests that a comparable real disk in the 55 Cnc images should have been seen with a signal to noise ratio (S/N) of about 65. This recovered flux density is also about 10 times higher than the dispersion in the scattered-light background amongst all our measures (Table 4). Given this, we would have expected to detect an integrated flux excess from the suggested disk in our PSF subtracted images.

The azimuthally averaged brightness profiles were also measured from the disk-implanted images, and their statistical errors were assessed. In all cases the model disk was recovered in the presence of the noise in the observations at the levels indicated by the superposition of the measured subtractions as given in Table 4 with a disk of integrated flux density 8.2 mJy. For example, in Figure 6 we show this for the subtraction of the visit 60 image of 55 Cnc using the HD 75216 reference PSF for comparison with the null results already discussed in concert with Figure 4. The implanted disk with an integrated S/N of  $\sim 80$  is readily apparent. As for Figure 4, the error bars for Figure 6 indicate the standard deviations of all pixels about the mean,  $\sigma(N)$ , of each 1 AU wide annulus [ $\sim 2$  to  $1 \sigma(N)$  for 28 to 42 AU, respectively]. If the residuals in the subtracted data smoothed with a three pixel kernel are otherwise spatially uncorrelated, the standard deviations of the means,

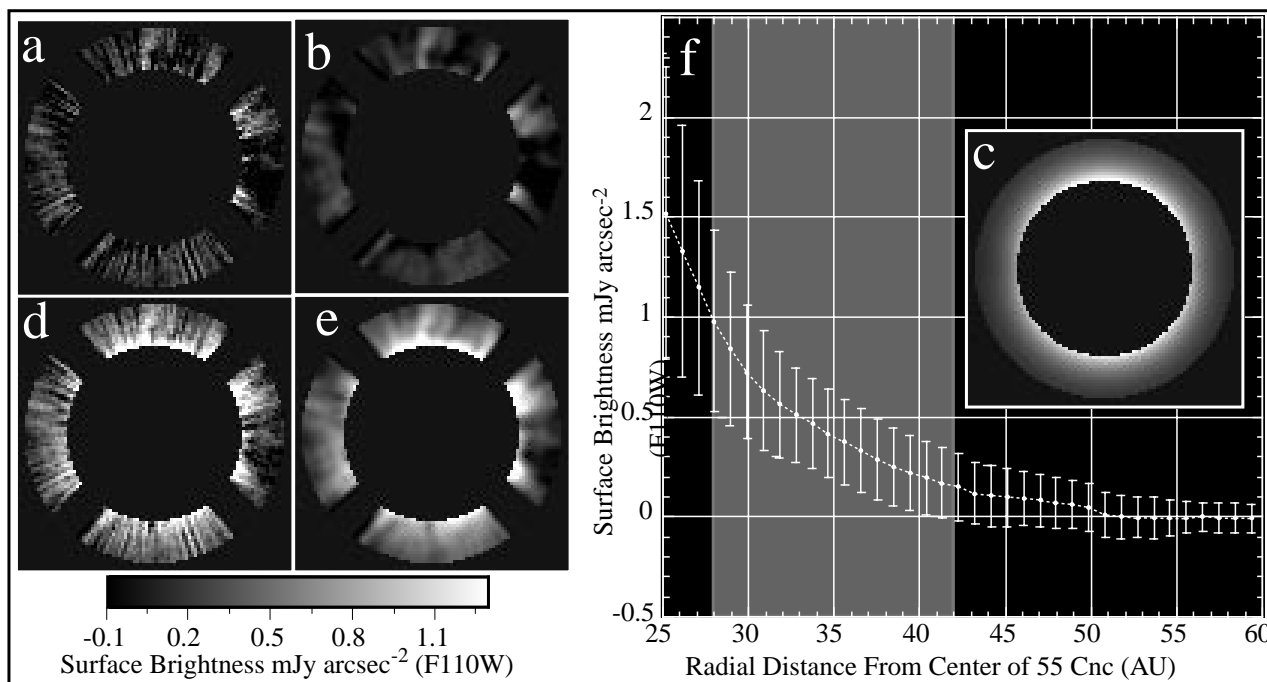


FIG. 6.—(a) Scaled PSF subtraction of 55 Cnc (visit 60) by HD 75216 (visit 62) in the annulus observed and fit by TB98 (28–42 AU zone). (b) Image (a) smoothed to remove high-frequency radially directed artifacts. (c) Axisymmetric  $r^{-5}$  model disk with flux density characteristics described by TB98. (d) Model disk (c) registered and implanted in subtraction (a) with major axis oriented as discussed by TB98 (along vertical axis in these data). (e) Image (d) smoothed as for image (b). (f) Surface brightness profile of implanted model disk the region discussed and fit by TB98 in gray. Error bars in (f) are the standard deviations of all unmasked pixels about the mean in 1 AU wide annular zones at the indicated radial distance. Panels (a)–(e) are shown at the same linear stretch as indicated by the scale bar. Data affected by *HST* diffraction spikes (along diagonals) were masked and excluded in measuring the surface brightness profile.

$\sigma(\text{mean})$ , would be reduced to  $\sim\sigma(N)/9$  in the 28 to 42 AU annular zone, giving rise to 18 to 9  $\sigma(\text{mean})$  detections in each of the corresponding zones. This is consistent with the assessment of our detection limits based upon the systematics in the PSF subtractions detailed in § 7.1.

### 9. AZIMUTHAL ANISOTROPY

TB98 reported an anisotropy in the surface brightness of the putative disk manifesting itself as a 1.7:1 ratio in flux densities measured in sectors oriented along the disk major axis (aligned at a position angle of  $\sim 45^\circ$ ) compared with the minor-axis flux. In our visit 60 image of 55 Cnc the major axis of the reported disk lies essentially in the vertical direction. Thus, if a disk as bright as suggested by TB98 was present, we could have observed a significant difference in the major to minor axis integrated flux densities. However, as the scattered-light component of the 55 Cnc disk actually appears to be at or below our detection limits, our data cannot meaningfully contribute to investigating the axial asymmetry suggested by TB98. We note, however that the azimuthal morphologies of our two 55 Cnc observations (visits 60 and 61), which were rotated  $15^\circ$  with respect to each other, are extremely similar (see Fig. 1), and both very closely resemble our null-star subtractions (for example, inset *a* of Fig. 3). The lack of differential azimuthal asymmetry in the two differently oriented 55 Cnc images, and their similarities to the comparative null images, further suggest that the integrated flux density we measure at the  $\sim 0.4$  mJy level (for our best PSF subtraction in the 28–42 AU zone) is likely instrumental in origin.

### 10. COMPARISON WITH OTHER NICMOS OBSERVATIONS

While the  $r^{-5}$  power law index reported for the putative 55 Cnc scattered light disk by TB98 is rather steep, the flux densities in specific regions at different radii are comparable to (and in some cases larger than) the positive NICMOS detections of material around other IR excess stars. In Figure 7 we compare the PSF-subtracted NICMOS coronagraphic image of the circumstellar environment of 55 Cnc (the null detection from visit 60 using HD 75216 as a PSF) to two other sources of similar spatial scales and surface brightnesses; TW Hya (Weinberger et al. 2000) and HD 141569 (Weinberger et al. 1999). The data from which

these images were obtained was reduced and processed in a manner similar to the 55 Cnc data. And, like 55 Cnc, several PSF stars were applied to each, yielding consistent morphological and photometric results. We present these images, along with quantitative assessments of our detection limits, as a demonstration of the efficacy of the NICMOS coronagraphic system in detecting and spatially resolving reflection disks with properties similar to those suggested for 55 Cnc by TB98.

From the TB98 results we would have expected an F110W azimuthally averaged surface brightness of 1 mJy arcsec $^{-2}$  at a radius of  $\sim 28$  AU (29 pixels in NICMOS camera 2). In panel (*a*) of Figure 7 (55 Cnc image) we indicate where this region is located. The dynamic range of this display is the same as that of the 55 Cnc image and the comparative images in panels (*b*) and (*c*), with the high-end (white) set to the anticipated level of the TB98 disk at 28AU (1 mJy arcsec $^{-2}$ ). As may be inferred from the analysis of our detection limits and model disk implantation experiment, this is rather far out from the residual glare of 55 Cnc, and we would expect a 1 mJy arcsec $^{-2}$  disk to have been readily seen at this radius. The zonal regions of comparable surface brightness in the TW Hya image and the inclined ring of maximum brightness around HD 141569 are closer in, in angular distance, primarily because of the greater distances to these stars. Since the apparent brightness of 55 Cnc exceeds both TW Hya and HD 141569 by at least an order of magnitude the residual amplitudes in the image artifacts around 55 Cnc at comparable radii are correspondingly larger. The amplitude and morphology of the scattered light residuals are very similar to those seen in the mutual subtractions of unresolved point sources of comparable brightness.

### 11. DISCUSSION

Our nondetection of near-IR scattered light from the circumstellar debris system in 55 Cnc is inconsistent with the flux densities and morphology of the surface brightness profile reported by TB98 and TBR2000. The discrepancy is significant at radii  $\gtrsim 28$  AU as discussed by TB98. It is also significant in the 19–28 AU zone more recently presented by TBR2000. Given the NICMOS 1.1  $\mu\text{m}$  sensitivities and detection limits, this interior region is effectively probed to a limiting distance of  $\sim 15$  AU with the NICMOS corona-

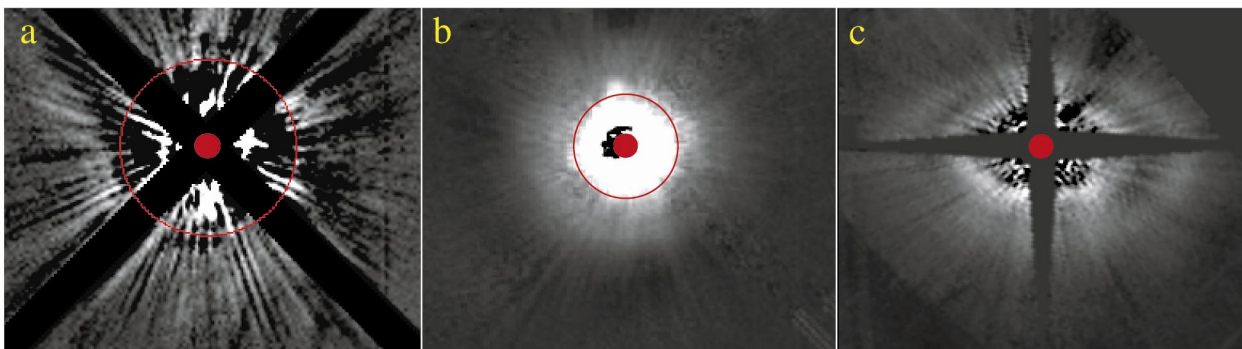


FIG. 7.—Comparative imaging of circumstellar material at  $1.1\mu\text{m}$  via PSF-subtracted NICMOS coronagraphy. (*a*) 55 Cnc ( $H = 4.17$ ) nondetection. (*b*) Face-on disk about the classical T Tauri star TW Hya ( $H = 7.34$ ). (*c*) Inclined debris disk circumscribing Herbig AeBe star HD 141569 ( $H = 6.89$ ). All panels are linear displays at the same stretch from  $-0.1$  to  $1.0$  mJy arcsec $^{-2}$  and presented at the same angular image scale. The red circles in (*a*) at a radius of  $2''.2$  (28 AU) and (*b*) at  $1''.3$  (65 AU), respectively, indicate the locations of the  $1.0$  mJy arcsec $^{-2}$  surface brightness contours expected from TB98 in 55 Cnc and observed for TW Hya. The bright ring at  $1''.85$  (185 AU) in (*c*) has an azimuthally averaged surface brightness of  $0.27$  mJy arcsec $^{-2}$ . The solid circles indicate the physical size of the NICMOS coronagraphic hole ( $0''.3$  radius).

graph, yet we detect no statistically significant circumferential flux excess in any of these regions.

### 11.1. Disparity in Scattered Light

*Near-IR.*—The NICMOS upper detection limits to the integrated scattered light at  $1.1\ \mu\text{m}$  are 10 to 20 times lower than the  $8.2\ \text{mJy arcsec}^{-2}$  level in the 28–42 AU circumstellar region suggested by TB98. Additionally, in the region interior to 28 AU as discussed by TBR2000, despite the presence of image artifacts induced by the *HST* + NICMOS optics close to the star, the NICMOS system sensitivity was sufficiently high to have detected a disk with a surface brightness at least ten times fainter than reported. Yet, none was seen.

*Mid-Far-IR.*—The mid-far-infrared optical depth for the disk around 55 Cnc is measured at  $\sim 6 \times 10^{-5}$  (Dominik et al. 1998; Jayawardhana et al. 2000). If the dust in the 55 Cnc disk is like that found around  $\beta$  Pictoris, HR 4796A and HD 141569, the albedo of the grains would be in the range  $0.2 \lesssim \omega \lesssim 0.5$ . Thus, the scattered-light optical depth at a given wavelength would be a few times smaller than the IR optical depth (e.g., for HD 141569  $L_{\text{IR}}/L_* = 8 \times 10^{-3}$  and  $F_{\text{scattered}}/F_* = 3 \times 10^{-3}$  at  $1.1\ \mu\text{m}$ ). For 55 Cnc we would therefore predict  $F_{\text{scattered}}/F_* = 1\text{--}5 \times 10^{-5}$  at  $1.6\ \mu\text{m}$ . At *H*-band, 55 Cnc is 4.17 mag (Persson et al. 1977) or 22.3 Jy, so the predicted disk flux would be  $\sim 0.38\ \text{mJy}$ . The TBR2000 surface brightness profile indicates a minimum scattered-light flux density of  $\sim 6.6\ \text{mJy}$  (integrating outward from their limiting radius of 19 AU),  $\sim 17$  times greater than expected and implying  $\tau_{\text{scatter}} = 3 \times 10^{-4}$ . This scattering fraction is more than an order of magnitude larger than observed in other disks. Assuming this large  $\tau_{\text{scatter}}$ , the albedo inferred is 0.83. This is not out of the realm of possibility for ice. We note, however, that it is higher than the albedo for the disks around (1) HR 4796A (0.2 combining Schneider et al. 1999 and Jura et al. 1998), (2) HD 141569 (0.3–0.5 from Weinberger et al. 1999), (3)  $\beta$  Pictoris (0.6 from Pantin, Lagage, & Artymowicz 1997), and more than an order of magnitude higher than the very dark 0.06 assumed by TB98 for Kuiper beltlike objects. While it is physically possible that such dust particles might exist, given the NICMOS results, it seems more reasonable that the flux density due to scattering by circumstellar grains is actually an order of magnitude or more lower than reported by TB98.

*Far-IR-Submillimeter.*—The absence of scattered NIR radiation in the NICMOS images from circumstellar dust, to the flux density limits previously discussed, in the  $19 < r < 42\ \text{AU}$  (the annular zone reported on by TB98 and TBR2000) is consistent with a model of the disk developed by Dominik et al. (1998) based upon ISO flux excesses. They found the 55 Cnc dust grains cannot exceed a temperature of 100 K, must be located at radii  $\gtrsim 35\ \text{AU}$  and are likely distributed in a zone 50–60 AU from the star. Fitting a blackbody spectral energy distribution to the far-IR and their more recent JCMT/SCUBA 450 and 850  $\mu\text{m}$  observations, JAY2000 suggest a central hole with  $r \lesssim 35\ \text{AU}$  for a dust temperature of 60 K (consistent with Dominik et al. 1998). They note that for grains as warm as 100 K the radius of the central hole could be as small as 13 AU. However, if the surface brightness reported by TB98 continued increasing inward of 28 AU with their suggested  $r^{-5}$  power law, the expected  $1.1\ \mu\text{m}$  surface brightness at 19 AU (reported on by TBR2000) would be  $\sim 8\ \text{mJy arcsec}^{-2}$ , easily detect-

able but not seen with NICMOS (Fig. 5). Such an inward extrapolation is almost certainly not warranted as the scattering properties of the dust would have to be radially isotropic. This is very unlikely as the albedo (for example) would have a strong dependence on radius as the ice sublimation temperature is reached (Pantin et al. 1997). Nonetheless, in the presence of a submillimeter disk with flux densities discussed by JAY2000, some amount of excess scattered-light flux would be expected closer to the star, but this must be below our detection limits as discussed in § 7.2.

### 11.2. Resolving the Disparities

As expected from the observed thermal and submillimeter fluxes, we are unable to confirm the detection of scattered near-IR light reported by TB98. There are two possibilities for our nondetection.

1. We feel that the most likely possibility is that the TB98 and TBR2000 detection is spurious. In this case, our nondetection places an upper limit to the  $1.1\ \mu\text{m}$  emission of at most  $\sim 10\%$  of the integrated spectral flux density in a disk with the properties reported by TB98. This possibility relieves the 1–2 order of magnitude discrepancy in the estimates of the dust mass inferred by TB98 and JAY2000. It also removes the need to invoke unusual grain properties and geometries in an attempt to explain the TB98 reported flux densities. This conjecture is supported by the fact that all three disks reported by TBR2000 have very similar morphologies and flux density distributions (i.e., surface brightness vs. radial distance in arcseconds) despite the lack of any thermal IR radiation in those systems as sampled by ISO.

2. The NICMOS data are faulty. However, given the extensive discussions in §§ 4–7, and our successful detection of disks of other systems of comparable brightness and spatial extent (e.g., Fig. 7), we reject this alternative.

## 12. CONCLUSIONS

Utilizing the NICMOS coronagraph on board *HST*, we have attempted to confirm and characterize the circumstellar debris disk surrounding 55 Cnc seen in scattered NIR light as reported by TB98. We find, however, no significant evidence for the existence of a near-IR excess, nor do we find any morphological structures resembling a disk, in our highest sensitivity (F110W) PSF subtracted images. The NICMOS observations indicate that any light scattered from a disk at  $1.1\ \mu\text{m}$  must be at least 10 (and likely 20) times fainter than suggested by TBR2000. The actual scattered flux could be even smaller, adding observational support to the conjecture by JAY2000 that TB98 may have overestimated the surface brightness of a scattered light disk. This conjecture should be tested by additional NIR observations designed to set more stringent limits on the brightness and morphology of a disk which may be seen in reflected light.

We are unable to account for the disparity in the NICMOS and CoCo observations. We cautiously suggest that the flux excess seen by TB98 may have been spurious as a result of the difficulties involved in ascribing the correct amount of flux to subtract via a scaled PSF. Further CoCo observations are required to resolve the disparity in these two data sets. To help resolve this, we advocate cross-correlating NICMOS and CoCo coronagraphic data sets. We suggest the need for observations of well-characterized

and independently confirmed NICMOS scattered light disks such as TW Hya (also seen in the optical with WFPC-2 by Krist et al. 1998) and HD 141569 (independently observed with NICMOS by Augereau et al. 1999) with the CoCo system.

We gratefully acknowledge the many contributions by the other members of the NICMOS Environments of Nearby Stars and Instrument Definition Teams during the course of

this investigation. We also thank our program coordinator, Douglas Van Orsow, and contact scientist, Alfred Schultz, at STScI for the assistance in the last-minute scheduling and implementation of these observations. This work is supported by NASA grant NAG 5-3042. This paper is based on observations with the NASA/ESA *Hubble Space Telescope*, obtained at the Space Telescope Science Institute, which is operated by the Association of Universities for Research in Astronomy, Inc., under NASA contract NAS 5-26555.

## REFERENCES

- Augereau, J. C., Lagrange, A. M., Mouillet, D., & Menard, F. 1999, *A&A*, 350, L51
- Aumann, H. H. 1985, *PASP*, 97, 885
- Baliunas, S., Henry, G. W., Donaheau R. A., Fekel F. C., & Soon, W. H. 1997, *ApJ*, 474, L119
- Bely, P. 1993, STScI Report (SESD-93-16) (Baltimore: STScI)
- Butler, R. P., Marcy, G. W., Williams, E., Hauser, H., & Shirts, P. 1997, *ApJ*, 474, L115
- Cowley, A. P., Hiltner, W. A., & Witt, A. N. 1967, *AJ*, 72, 1334
- Dominik, C., Laureijs, R. J., Jourdain de Muizon, M., & Habing, H. J. 1998, *A&A*, 329, L53
- Fuhrmann, K., Pfeiffer, M. J., & Bernkopf, J. 1998, *A&A*, 336, 942
- Gonzalez, G. 1998, *A&A*, 334, 221
- Gonzalez, G., & Vanture, A. D. 1998, *A&A*, 339, L29
- Greaves, J. S., et al. 1998, *ApJ*, 506, L133
- Jayawardhana, R., Holland, W., Greaves, J., Dent, W., Marcy, G., Hartmann, L., & Giovanni, G. 2000, *ApJ*, 536, 425
- Jura, M., Malkan, M., White, R., Telesco, C., Pina, R., & Fisher, R. S. 1998, *ApJ*, 505, 897
- Kant, I. 1755, *Allgemeine Naturgeschichte und Theorie des Himmels* (Leipzig: Petersen)
- Krist, J. E., Golimbowski, D. A., Schroeder, D. J., & Henry, T. J. 1998, *PASP*, 110, 1046
- Kulkarni, V. P., Hill, J. M., Schneider, G., Weymann, R. J., Storrie-Lombardi, L. J., Rieke, M. J., Thompson, R. I., & Jannuzi, B. 2000, *ApJ*, 536, 36
- Laplace, P.-S. 1796, in *Exposition du systeme du monde* (Paris: de l'Impr. Cercle-Social)
- Lowrance, P. J., et al. 1998, in *NICMOS and the VLT: A New Era of High-Resolution Near-Infrared Imaging and Spectroscopy*, ed. W. Freudling & R. Hook (Garching: ESO), 96
- Lytle, D., Stobie, E., Ferro, A., & Barg, I. 1999, in *ASP Conf. Ser. 172, Astronomical Data Analysis Software and Systems 8*, ed. D. M. Mehringer, R. L. Plante, & R. A. Roberts (San Francisco: ASP), 445
- Mackenty, J. 1997, *NICMOS Instrument Handbook* (Baltimore: STScI)
- Marcy, G. W., & Butler, R. P. 1994, in *ASP Conf. Ser. 64, Eighth Cambridge Workshop*, ed. J.-P. Caillault (San Francisco: ASP), 587
- Marlborough, J. M. 1964, *AJ*, 69, 215
- Nikonov, V. B., Nekrasova, S. V., Polosukhina, N. S., Rachkovsky, N. D., & Chuvajec, W. K. 1957, *Izv. Krym. Astrofiz. Obs.*, 17, 42
- Pantin, E., Lagage, P. O., & Artymowicz, P. 1997, *A&A*, 327, 1123
- Park, S., & Schowengerdt, R. 1983, *Comput. Vision, Graphics, and Image Processing*, 23, 256
- Persson, S. E., Aaronson, M., & Frogel, J. A. 1977, *AJ*, 82, 729
- Schneider, G. 1998a, in *NICMOS and the VLT: A New Era of High-Resolution Near-Infrared Imaging and Spectroscopy*, ed. W. Freudling & R. Hook (Garching: ESO), 88
- Schneider, G., Thompson, R. I., Smith, B. A., & Terrile, R. J. 1998b, in *Proc. SPIE*, 3356, 222
- Schneider, G., et al. 1999, *ApJ*, 513, L127
- Schultz, A., Storrs, A. D., & Fraquelli, D. 1999, *NICMOS Instrum. Sci. Rep. (ISR-99-006)* (Baltimore: STScI)
- Smith, B. A., & Terrile, R. J. 1984, *Science*, 226, 1421
- Toomey, D. W., Ftaclas, C., Brown, R. H., & Trilling, D. 1998, *Proc. SPIE*, 3354, 782
- Trilling, D. E., & Brown, R. H. 1998, *Nature*, 395, 775 (TB98)
- Trilling, D. E., Brown, R. H., & Rivkin, A. S. 2000, *ApJ*, 529, 499 (TBR2000)
- Weinberger, A. J., Becklin, E. E., Schneider, G., Smith, B. A., Lowrance, P. J., Silverstone, M. D., & Zuckerman, B. 1999, *ApJ*, 525, L53
- Weinberger, A. J., Schneider, G., Silverstone, M., Becklin, E. E., Smith, B. A., & Hines, D. C. 2000, in preparation